permafrost cci

CCI+ PHASE 2 – NEW ECVS

PERMAFROST

CCN4 OPTION 7

ICEINSAR: INFERRED ACTIVE LAYER WATER/ICE CONTENT AND FREEZE-THAW PROGRESSION FROM ASSIMILATING INSAR IN PERMAFROST MODEL

D4.1 PRODUCT VALIDATION AND INTERCOMPARISON REPORT (PVIR)

VERSION 1.0

30 SEPTEMBER 2024

PREPARED BY

b·geos GAMMA REMOTE SENSING

NORCE UiO : University of Oslo

Document Status Sheet

Issue	Date	Details	Authors
1.0	30.09.2024	First version	LW, LR, SW, AB, TS

Author team

Lotte Wendt and Line Rouyet, NORCE

Sebastian Westermann, UiO

Annett Bartsch, B.GEOS

Tazio Strozzi, GAMMA

ESA Technical Officer

Frank Martin Seifert

EUROPEAN SPACE AGENCY CONTRACT REPORT

The work described in this report was done under ESA contract.
Responsibility for the contents resides in the authors or organizations that prepared it.

Table of contents

Executive summary

Within the European Space Agency (ESA), the Climate Change Initiative (CCI) is a global monitoring program which aims to provide long-term satellite-based products to serve the climate modelling and climate user community. The two main products associated to the ECV Permafrost are Ground Temperature (GT) and Active Layer Thickness (ALT). GT and ALT are documented by the Permafrost_cci project based on thermal remote sensing and physical modelling.

The Permafrost_cci models take advantage of additional datasets, such as snow cover and land cover, to estimate the heat transfer between the surface and the underground. However, several challenges remain due to spatially variable subsurface conditions, especially in relation to unknown amounts of water/ice in the active layer that modify the effective heat capacity and the thermal conductivity of the ground. In complex terrain with large spatial heterogeneities, coarse and partly inadequate land cover categorisation, the current results show discrepancies with in-situ measurements, which highlight the need to assimilate new data sources as model input. Although the ground stratigraphy is not directly observable from space, it impacts the dynamics of the ground surface. The seasonal thawing and refreezing induce cyclic subsidence and heave of the ground surface due to ice formation and melt in the active layer, and can therefore be used as indirect indicator of the ground conditions.

Synthetic Aperture Radar Interferometry (InSAR) based on Sentinel-1 images can be used to measure the amplitude and seasonal progression of these displacements. The movement amplitude is related to the amount of water/ice that is affected by a phase change, whilst the timing of the displacement patterns reflects the vertical progression of the thawing/freezing front. Considering the fine to medium spatial resolution of Sentinel-1 images, InSAR time series therefore have the potential to enhance the characterisation of subsurface hydrogeologic and thermal parameters and adapt the existing Permafrost_cci models to improve their performance at the local to regional scale. The *IceInSAR* pilot project (Option 7) will develop a prototype for permafrost model adjustment by assimilating Sentinel-1 InSAR surface displacement maps and time series into the model to constrain stratigraphy parameters. *IceInSAR* will provide pilot products, expected to be used for adjustment of the ECV processing chain of the baseline project in a next phase.

This Product Validation and Intercomparison Report (PVIR) evaluates the results of the *IceInSAR* Option 7 results described in the Climate Research Data Package (CRDP) [RD-1], using the uncertainty assessment methods and in-situ validation data, previously described in the Product Validation Plan (PVP) [RD-8].

1 Introduction

1.1 Purpose of the document

This document assesses the quality and relevance of the results of the *IceInSAR* Option 7. It has to be read together with the CRDP [RD-1] and the PUG [RD-2].

1.2 Structure of the document

Section 2 assesses the quality of the in-situ data. Section 3 assesses the quality of the InSAR results. Section 4 assesses the quality of the model simulations. Section 5 presents the comparison between InSAR, in-situ and modelling results. Section 6 summarizes the conclusions of the study and discusses ideas for future Permafrost_cci developments. Section 7 includes a bibliography and list of acronyms. A glossary of the commonly accepted permafrost terminology can be found in RD-15.

1.3 Applicable Documents

[AD-1] ESA. 2022. Climate Change Initiative Extension (CCI+) Phase 2 – New Essential Climate Variables – Statement of Work. ESA-EOP-SC-AMT-2021-27.

[AD-2] GCOS. 2022. The 2022 GCOS Implementation Plan. GCOS – 244 / GOOS – 272. Global Observing Climate System (GCOS). World Meteorological Organization (WMO).

[AD-3] GCOS. 2022. The 2022 GCOS ECVs Requirements. GCOS – 245. Global Climate Observing System (GCOS). World Meteorological Organization (WMO).

1.4 Reference Documents

[RD-1] Wendt, L., Rouyet, L., Westermann, S., Bartsch, A., Strozzi, T. 2024. ESA CCI+ Permafrost Phase 2. CCN4 Option 7. IceInSAR: Inferred Active Layer Water/Ice Content and Freeze-Thaw Progression From Assimilating InSAR in Permafrost Model. D.3.2 Climate Research Data Package (CRDP). Version 1.0. European Space Agency.

[RD-2] Wendt, L., Rouyet, L., Westermann, S., Bartsch, A., Strozzi, T. 2024. ESA CCI+ Permafrost Phase 2. CCN4 Option 7. IceInSAR: Inferred Active Layer Water/Ice Content and Freeze-Thaw Progression From Assimilating InSAR in Permafrost Model. D.4.2 Product User Guide (PUG). Version 1.0. European Space Agency.

[RD-3] Rouyet, L., Wendt, L., Westermann, S., Bartsch, A., Strozzi, T. 2023. ESA CCI+ Permafrost Phase 2. CCN4 Option 7. IceInSAR: Inferred Active Layer Water/Ice Content and Freeze-Thaw Progression From Assimilating InSAR in Permafrost Model. D.1.1 User Requirement Document (URD). Version 1.0. European Space Agency.

[RD-4] Rouyet, L., Wendt, L., Westermann, S., Bartsch, A., Strozzi, T. 2023. ESA CCI+ Permafrost Phase 2. CCN4 Option 7. IceInSAR: Inferred Active Layer Water/Ice Content and Freeze-Thaw Progression From Assimilating InSAR in Permafrost Model. D.1.2 Product Specification Document (PSD). Version 1.0. European Space Agency.

[RD-5] Rouyet, L., Wendt, L., Westermann, S., Bartsch, A., Strozzi, T. 2023. ESA CCI+ Permafrost Phase 2. CCN4 Option 7. IceInSAR: Inferred Active Layer Water/Ice Content and Freeze-Thaw

Progression From Assimilating InSAR in Permafrost Model. D.2.2 Algorithm Theoretical Basis Document (ATBD). Version 1.0. European Space Agency.

[RD-6] Rouyet, L., Wendt, L., Westermann, S., Bartsch, A., Strozzi, T. 2023. ESA CCI+ Permafrost Phase 2. CCN4 Option 7. IceInSAR: Inferred Active Layer Water/Ice Content and Freeze-Thaw Progression From Assimilating InSAR in Permafrost Model. D.2.3 End-to-End ECV Uncertainty Budget (E3UB). Version 1.0. European Space Agency.

[RD-7] Rouyet, L., Wendt, L., Westermann, S., Bartsch, A., Strozzi, T. 2023. ESA CCI+ Permafrost Phase 2. CCN4 Option 7. IceInSAR: Inferred Active Layer Water/Ice Content and Freeze-Thaw Progression From Assimilating InSAR in Permafrost Model. D.2.4 Algorithm Development Plan (ADP). Version 1.0. European Space Agency.

[RD-8] Rouyet, L., Wendt, L., Westermann, S., Bartsch, A., Strozzi, T. 2023. ESA CCI+ Permafrost Phase 2. CCN4 Option 7. IceInSAR: Inferred Active Layer Water/Ice Content and Freeze-Thaw Progression From Assimilating InSAR in Permafrost Model. D.2.5 Product Validation Plan (PVP). Version 1.0. European Space Agency.

[RD-9] Bartsch, A., Matthes, H., Westermann, S., Heim, B., Pellet, C., Onaca, A., Strozzi, T., Kroisleitner, C., Strozzi, T. 2023. ESA CCI+ Permafrost Phase 2. D.1.1 User Requirement Document (URD). Version 3.0. European Space Agency.

[RD-10] Bartsch, A., Westermann, S., Strozzi, T., Wiesmann, A., Kroisleitner, C., Wieczorek, M., Heim, B. 2023. ESA CCI+ Permafrost Phase 2. D.1.2 Product Specification Document (PSD). Version 3.0. European Space Agency.

[RD-11] Westermann, S., Bartsch, A., Strozzi, T. 2023. ESA CCI+ Permafrost. D.2.2 Algorithm Theoretical Basis Document (ATBD). Version 4.0. European Space Agency.

[RD-12] Westermann, S., Bartsch, A., Strozzi, T. 2023. ESA CCI+ Permafrost. D.3.2 Climate Research Data Package (CRDP). Version 4.0. European Space Agency.

[RD-13] Bartsch, A., Obu, J., Westermann, S., Strozzi, T. 2024. ESA CCI+ Permafrost. D.4.3 Product User Guide (PUG). Version 4.1. European Space Agency.

[RD-14] Heim, B., Wieczorek, M., Pellet, C., Delaloye, R., Bartsch, A., Strozzi, T. 2024. ESA CCI+ Permafrost. D.4.1 Product Validation and Intercomparison Report (PVIR). Version 4.0. European Space Agency.

[RD-15] van Everdingen, Robert, Ed. 1998 revised May 2005. Multi-language glossary of permafrost and related ground-ice terms. Boulder, CO: National Snow and Ice Data Center/World Data Center for Glaciology (http://nsidc.org/fgdc/glossary/; accessed 23.09.2009).

1.5 Bibliography

A complete bibliographic list that supports arguments or statements made within the current document is provided in Section 7.1.

1.6 Acronyms

A list of acronyms is provided in Section 7.2.

2 In-situ data – quality assessment

The in-situ data consists of the ground ice contents from cores acquired at 12 sites and the Active Layer Thickness (ALT) based on thaw depth manual probing at similar locations. The ground ice contents (pore and excess ice) have been used to calculate the expected subsidence of the ground surface upon thawing of the active layer (see CRDP [RD-1]).

There are several identified limitations regarding the field measurements:

- The length of the core sections was compared to the borehole depth. However, it was not always possible for distributed sections. 7 m out of 16.5 m of core length were retrieved disturbed. For these sections, uncertainties of the core length must be expected.
- With the objective to document the ground conditions directly comparable with the following InSAR-documented season, the drilling campaign was performed as late as possible before thawing. Nevertheless, there might have still been some changes in the ground ice content afterwards.
- Drilling through gravel layers can generate heat that may cause ice to melt away (Subedi et al., 2020), which may have led to an unquantified uncertainty in the ground ice contents.
- The laboratory work is limited in the depth resolution and exposed to human errors. Non-destructive methods, such as X-ray computed tomography or gamma attenuation core logging (Nitzbon et al., 2022; Pumple et al., 2024) were not available for this work.
- A greater number of sites would have been valuable for a more robust statistical analysis, but the extensive labour required for core extraction and analysis made it impossible.

The in-situ uncertainties have been estimated as followed:

- The uncertainties of diameter and length of each core section are estimated to ± 0.2 cm.
- The dry weight uncertainty and wet weight uncertainty are estimated to ± 0.01 g based on the accuracy of the scale.
- The supernatant water volume uncertainty is estimated to ± 1 ml for volumes ≥ 2 ml.
- The uncertainty in the in-situ ALT was estimated to ± 5 cm.
- The uncertainty in the expected subsidence was estimated by propagating the individual measurement uncertainties. It is shown with error bars (whiskers) on Figure 7.

3 InSAR data – quality assessment

InSAR is affected by several error sources (see E3UB [RD-6]). However, the error quantification is a challenging task, especially in permafrost regions. No in-situ displacement measurement is available in the study area, which makes direct validation impossible.

The standard deviation of the retrieved displacements can be estimated based on the number of interferograms and the maximal temporal baseline used for the processing. Based on 60–80 interferograms and 48 days of maximal temporal baseline, the detection capability when using a simple averaging method (stacking) can be estimated to 1.4–1.6 mm/summer (Emardson et al., 2003). In 2023, however, significantly fewer interferograms could be included due to fast movement and the 12d repeat-pass of Sentinel-1. A 24d maximal baseline was applied and 13 interferograms were used. Based on Emardson et al. (2023), the theoretical uncertainty estimate increases to 6.9 mm/season.

Uncertainty values can also be estimated based on the results of other studies comparing InSAR and GNSS displacements (e.g. Yalvac, 2020; Cigna et al., 2021; Jiang and Lohman, 2021; Li et al., 2022). In addition, the effect of specific error sources can be estimated based on past research. For instance, Zwieback et al. (2017) has shown that the modification of dielectric ground properties from changes in soil moisture can affect the InSAR displacements by up to 10–20%. Based on these past studies, a conservative uncertainty estimate of ± 10 mm/season has been used in this study. It is shown with error bars (whiskers) on Figure 7. This value corresponds to a factor of 6 smaller than the mean seasonal subsidence magnitude in 2023 (Wendt, 2024).

An important source of error in InSAR time series is phase aliasing which may occur when the displacement exceeds a quarter the wavelength during the time interval used to build the SAR image pairs (see E3UB [RD-6]). Phase aliasing is more likely to affect areas/periods with fast movement and seasons during which only one Sentinel-1 satellite provides SAR images (12d repeat-pass). In Figure 1, we show the effect of one missing acquisition (08.08.2023) in ascending geometry, which lead to larger temporal baseline (24d) and phase aliasing at the end of summer. For this reason, the study focused on the results processed with images from the descending orbit. In Figure 2, we show the effect of increasing the minimal temporal baseline. The example is based on the 2020 season for which both Sentinel-1A and 1B were functional. The red line shows the SBAS results using both 6d and 12d high-coherent interferograms. The blue line simulates the effect of losing one satellite (12d interferograms only). The results show that the trends are similar. However, short-term patterns are less obvious (loss of temporal resolution) and the 12d minimal temporal baseline leads to a systematic underestimation of the results (Figure 3). Due to the failure of Sentinel 1B in 2021, the 2023 InSAR results used in the Option 7 are based on 12d only. We can therefore assume that the results are slightly underestimated.

As an estimate of the phase standard deviation (Balmer & Hartl, 1998), the interferometric coherence provides a measure of the InSAR uncertainty. The closest to 0 or 1, the lowest or highest the signal quality, respectively. The temporal variability of the InSAR quality can be documented through interferometric coherence time series. The coherence is averaged for all interferograms used for each considered acquisition time, which provide a time series comparable with the InSAR displacement time series. Figure 4 exemplifies such product for 2020 time series. It shows high signal quality in mid and late summer due to stable and dry ground conditions. The signal quality decreases at the beginning and end of the season, due to wet surface conditions and fast movement.

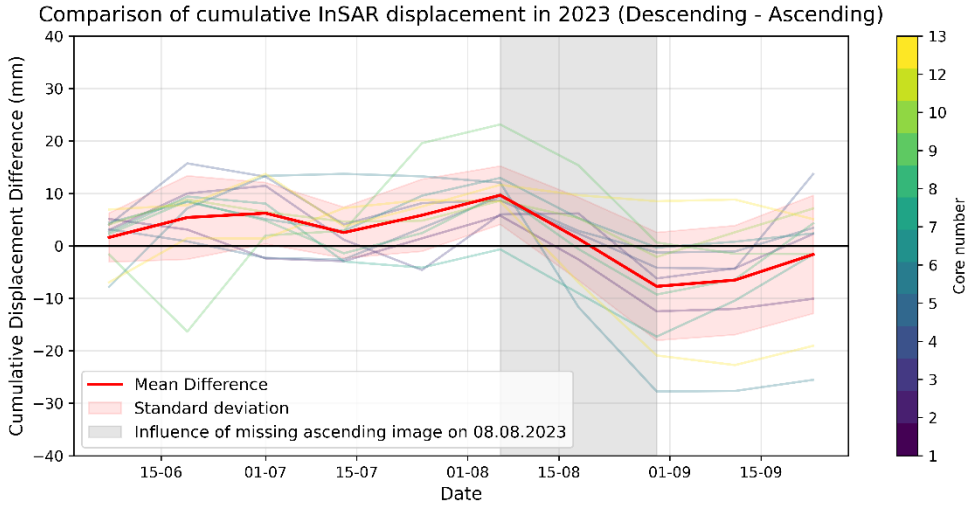

Figure 1: Comparison between 2023 InSAR results based on ascending and descending orbits. The plot displays the displacement difference between the two geometries (descending-ascending) for each descending acquisition. The ascending displacement at these times is linearly interpolated. Each line represents one coring site, with the mean difference and standard deviation shown in red. Note the influence of the missing ascending acquisition in August (grey area), which causes displacement underestimation. From Wendt (2024).

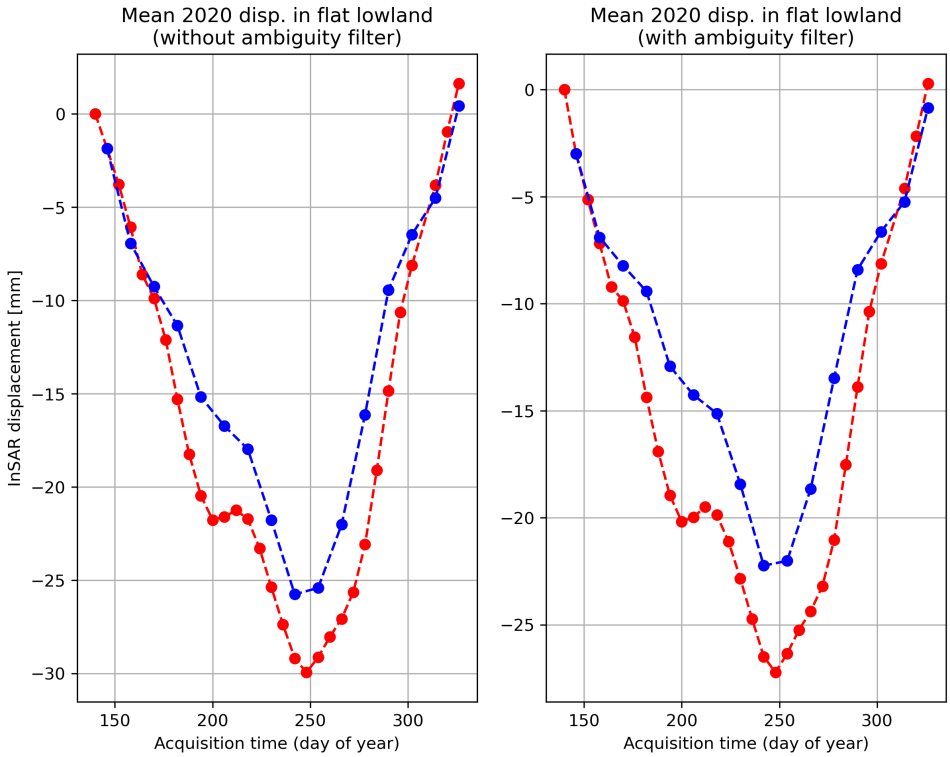

Figure 2: Example of InSAR displacement time series using 6d minimal temporal baseline in 2020 (red line), compared to time series simulating the effect of Sentinel-1B failure and the resulting increase of the minimal temporal baseline to 12d (blue line). Left: Mean displacement in flat lowland (Adventdalen, Svalbard), without additional filter. Right: Mean displacement in flat lowland (Adventdalen, Svalbard), filtering out pixels likely to be affected by phase ambiguities (displacement exceeding a quarter the wavelength between consecutive acquisitions).

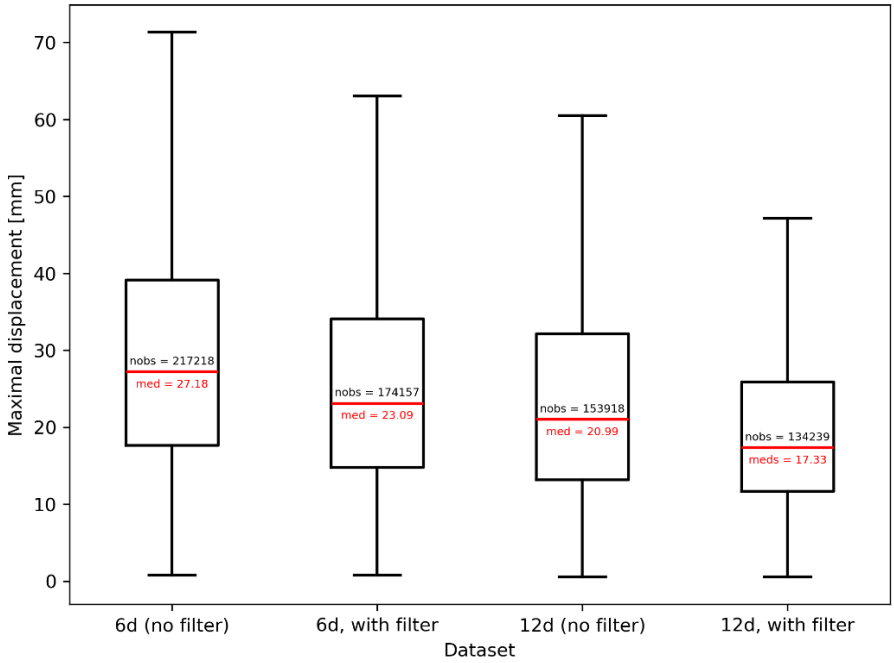

Figure 3: Boxplots showing the distribution of the maximal seasonal displacement in the flat valley bottom of Adventdalen, with 6–12d minimal temporal baseline and with/without phase ambiguity filter (as described in Figure 1 caption).

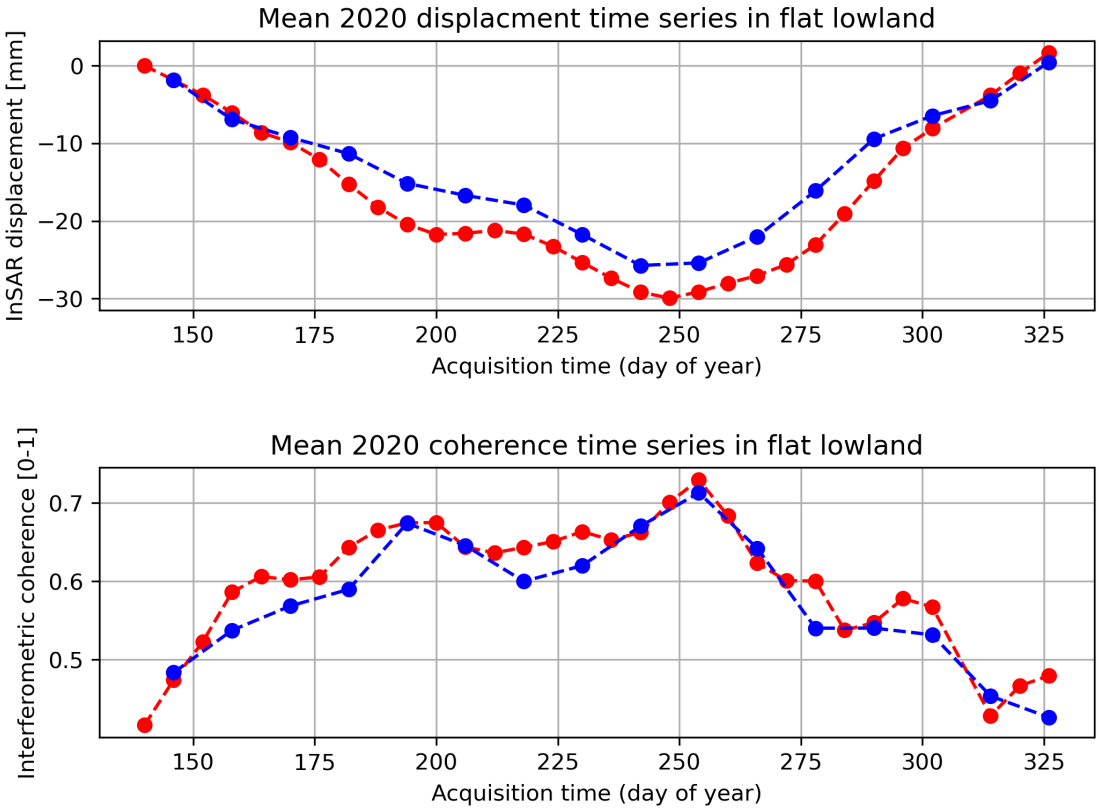

Figure 4: Example of InSAR displacement time series (similar as Figure 1, left) and the corresponding interferometric coherence time series during the snow-free 2020 season, in Adventdalen, Svalbard. Using 6d (red line) or 12d (blue line) minimal temporal baseline.

4 Model outputs – quality assessment

The quality of the model outputs with respect to the simulated subsurface stratigraphy depends on the calibration based on in-situ measurements. The pore ice model could be well calibrated based on the in-situ data, as the main ground stratigraphy parameters were available (e.g. soil type, organic matter content, ground ice content, porosity, field capacity). However, some of the model parameters (e.g. parameters related to the drainage conditions) were not directly accessible from in-situ data and were instead determined with a best-fit approach.

The excess ice model is still in a prototype stage and thus has some experimental components (Aga et al., 2023). Calibration tests show large variability in ground ice dynamics depending on soil type lateral parametrization, void ratio and permeability. Figure 5 displays two examples of the large variability of the simulated displacement time series depending on changes of the permeability values and water reservoir distance. It emphasizes that certain model parameters, which are difficult to constrain, can significantly affect the model outputs, and not always in a linear manner. However, it is expected that the uncertainties in such model parameters will be reduced when the model is applied at more sites.

In term of temporal representativity, the spin-up period of the model runs is somewhat short, as the initial temperature and ground ice profiles are based on in-situ measurements from 2023. In term of spatial representativity, the model forcing was downscaled through bias-correction with in-situ air temperature. Despite the small study area, a potential variability of climate conditions within the region might not have been captured.

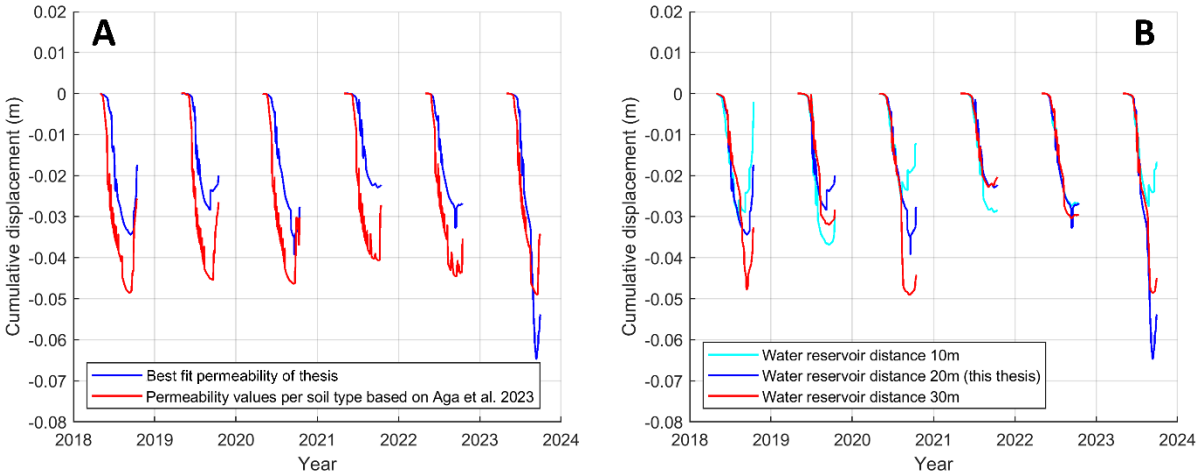

Figure 5: A. Variability of simulated displacement depending on the permeability parameter in the excess ice model. B. Variability of the simulated displacement depending on the water reservoir distance in the excess ice model. From Wendt (2024).

5 Product intercomparison

5.1 InSAR and in-situ comparison

For the comparison, the InSAR pixels closest to the coring sites were extracted. The disparity in spatial scales (point-scale for in-situ measurements vs approx. 30m InSAR pixel resolution) is an intrinsic limitation of such comparison. To account for uncertainties, a Monte Carlo approach was used to compare the 2023 InSAR seasonal subsidence with the expected subsidence calculated based on the in-situ ground ice content. Normally distributed random errors were introduced, and simulations repeated 1000 times to reflect the uncertainty of the respective measurements (see Sections 2 and 3).

The comparison between InSAR displacement and expected subsidence from in-situ shows that the observed subsidence cannot be explained without accounting for the melt and draining of the excess ice. Excess ice content is very variable across the measurement sites. At most sites, the excess ice melt (including drainage) is the main contributor of the 2023 subsidence (Figure 6).

InSAR-measured and expected subsidence are well correlated (Figure 7). Using a Monte-Carlo simulation, the effect of the uncertainty over 1000 random iterations leads to a mean r of 0.82, a mean R^2 of 0.68 and a mean absolute error of 15 mm. The relationship is statistically significant (p-value < 0.01). On the contrary, the correlation between InSAR and ALT is weak (R^2 = 0.03, r = -0.17, p-value = 0.60), which aligns with the results of the comparison between the expected subsidence and the ALT (see CRDP [RD-1]).

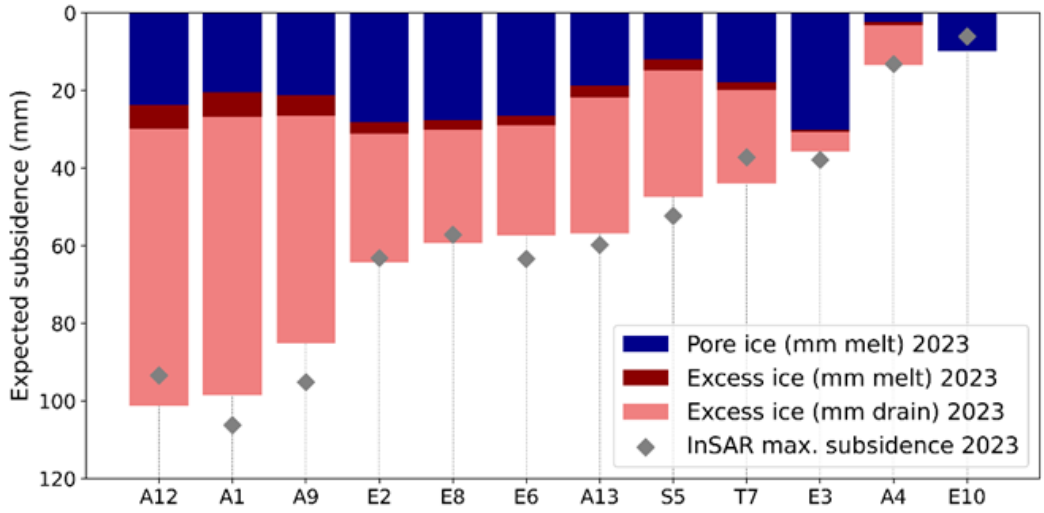

Figure 6: Contribution of pore ice melt, excess ice melt and excess ice meltwater drainage to the total expected subsidence at the different coring sites. The measured InSAR subsidence at similar locations is shown with the grey diamonds. From Wendt (2024).

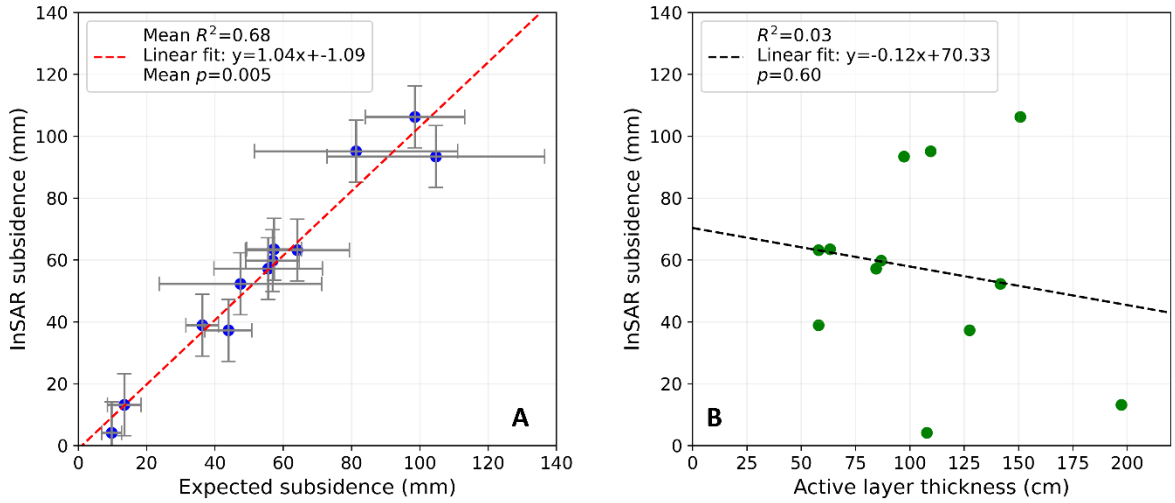

Figure 7: A. Relationship between the InSAR subsidence and the total expected subsidence (pore ice melt + excess ice melt + drainage). B. Relationship between the InSAR subsidence and the in-situ ALT. From Wendt (2024).

5.2 InSAR and model comparison

The comparison between the modelled time series and the InSAR observations focused on two sites with various ground conditions. In-situ data is used for model initialization and the closest InSAR pixels were extracted for comparison.

At the dry site (E10), the pore ice model aligns well with both the in-situ data and the InSAR time series (Figure 8). At the wet site (E2), the modelled ALT development generally aligns with the in-situ data. However, the pore ice model does not manage to replicate the InSAR displacement, especially in warm seasons (Figure 9). This indicates that the subsidence is likely caused by the top-of-permafrost melt of excess ice that the standard model scheme is not accounting for. Using the segregation ice model, the modelled displacement time series align better with the observed displacements (Figure 10A). The improvement is especially visible for warm seasons, such as 2023 (Figure 10B).

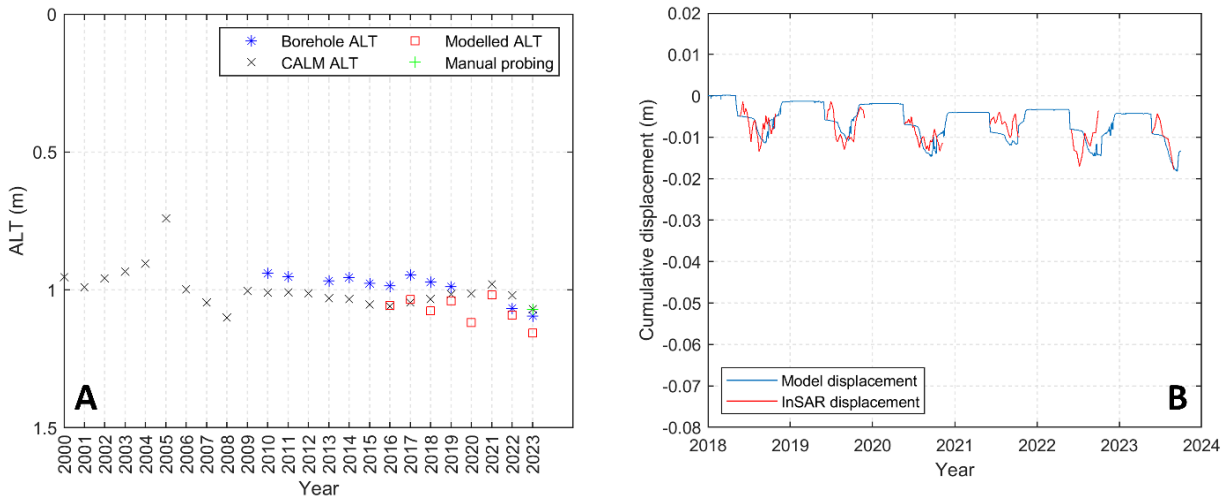

Figure 8: A. Active Layer Thickness (ALT) from the pore ice model, compared to the in-situ measurements at the dry site (E10). B. Simulated subsidence from the pore ice model, compared to the InSAR displacement time series at the dry site (E10). From Wendt (2024).

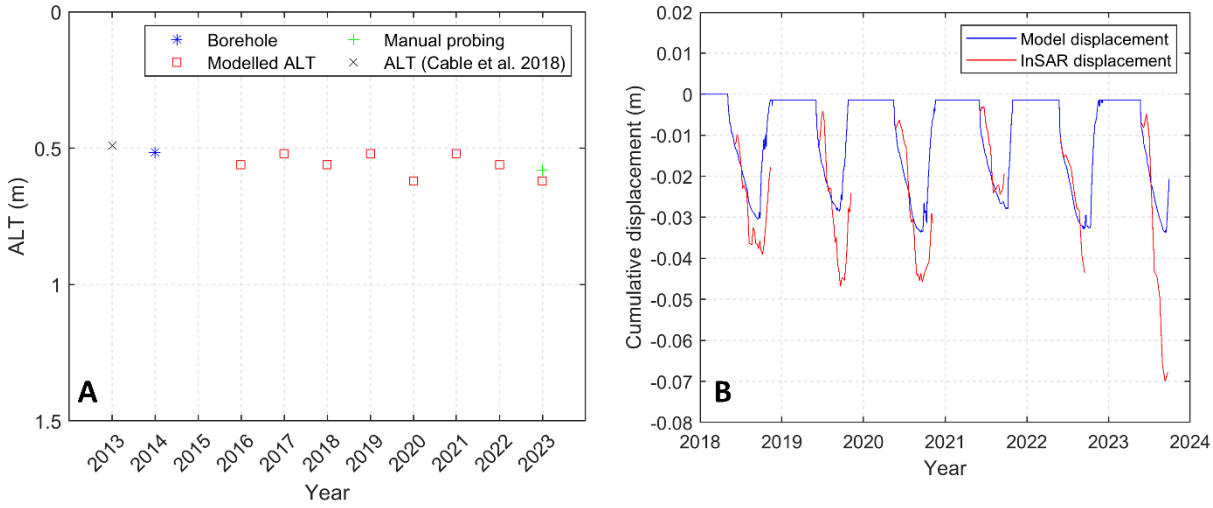

Figure 9: A. Active Layer Thickness (ALT) from the pore ice model, compared to the in-situ measurements at the wet site (E2). B. Simulated subsidence from the pore ice model, compared to the InSAR displacement time series at the wet site (E2). From Wendt (2024).

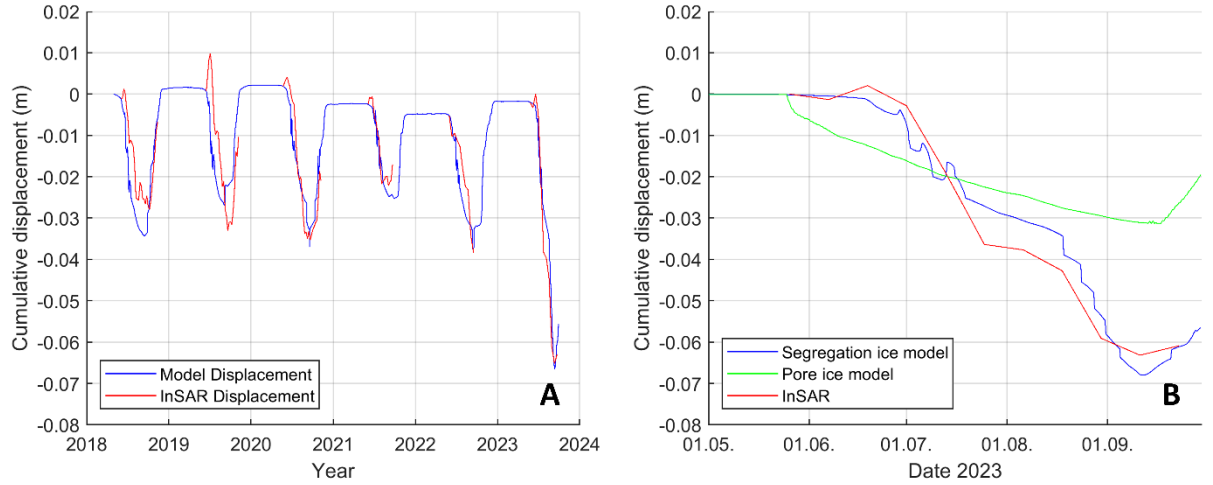

Figure 10: A. Simulated subsidence from the excess ice model, compared to the InSAR displacement time series at the wet site (E2). B. Detailed view of the warm 2023 season, comparing InSAR displacement and the results from both models. From Wendt (2024).

6 Conclusion and prospects

The *IceInSAR* pilot study confirms the **ability of InSAR to infer information on the spatial and vertical variability of ground ice contents**. The results from Section 5 show the good correlation between the InSAR displacements and the expected subsidence derived from the in-situ ice contents. The study also shows that standard pore ice model schemes not accounting for excess ice dynamics (as used in the Permafrost_cci baseline algorithm) fail to represent the surface elevation changes, especially for warm seasons during which the excess ice at the base of the active layer might melt.

IceInSAR results clearly show that InSAR holds **potential for constraining the parametrization of the ground stratigraphy in permafrost models**. Previous studies have shown that the assimilation of various remote sensing datasets improves the representation of factors controlling the active layer and permafrost thermal regime, for instance by documenting the snow cover (Aalstad et al., 2018) or the soil moisture (Zwieback et al., 2019). In the Permafrost_cci model, the ground stratigraphies are assigned based on landcover classes. However, this strategy leads to large uncertainties, since ground ice contents are difficult to parametrize due to high spatial variability, also within similar landcover classes. Over the past years, a significant effort has been placed on improving the input product (e.g. Option 6: Improved soil description through a landcover map dedicated for the Arctic; Bartsch et al., 2024a; b). The conclusions from the *IceInSAR* Option 7 provides new ideas to further this effort.

The pore-ice model configuration of the Permafrost_cci model is not able to represent the InSAR observations for the wet site. The results show a high sensitivity to excess ice that requires to consider ice segregation. In this respect, InSAR time series can indirectly help improving the model results by documenting the variability of the ice content in the active layer and the uppermost permafrost. The main challenge is to develop products providing key information to the model, while avoiding too computationally demanding ingestion strategies. Assimilation of the full-resolution InSAR time series is currently unrealistic, at least for large-scale applications. Instead, the **use of clustered products** should be investigated. One solution is to **assimilate the mean InSAR time series of each cluster**. However, even this simplified workflow is still computationally demanding especially for the excess ice model, so the first step forward is to associate **manually defined ground stratigraphy parameters** (ice-poor vs. ice-rich conditions) to each cluster based on user knowledge.

Another solution is to combine the information provided by InSAR with the landcover products currently used in the model, or under development in the Permafrost_cci project (Option 6). We expect that the landcover and InSAR products are both correlated and complementary. The landcover documents the spatial variability of the surface types that indirectly relates to the geological and hydrothermal conditions, while InSAR documents more directly the subsurface ice content. The information contained in InSAR can therefore be used to **refine the landcover categorization or develop new composite products**. In Figures 11–13, we show a first comparison between the Option 6 Permafrost_cci landcover products and InSAR displacement in Adventdalen, Svalbard. The proportion of the landcover classes within each InSAR cluster varies (Figure 12). As expected, the fraction of classes associated with moist conditions are more represented in clusters 0–3, corresponding to high subsidence rates (i.e. ice-rich conditions), while classes associated with dry conditions are more represented in clusters 3–4, corresponding to low subsidence rate (i.e. ice-poor conditions) (Figure 13). However, the wide range of classes included in each cluster also shows that the ground conditions are spatially variable within each landcover class. In this respect, InSAR may be able **to refine the**

subsurface parametrization of each landcover class. In the future, we see significant potential in developing **composite InSAR-landcover products** and test the impact on the model performance in selected regions. A natural first step in that direction is to systematically compare InSAR and landcover in several Arctic regions.

For global InSAR products over permafrost regions, efficient workflows for upscaling need to be developed. Further research is needed before InSAR technology reaches a maturity for systematic global coverage, but the development of large-scale InSAR operational services, such as the European Ground Motion Services (EGMS, https://egms.land.copernicus.eu/), show that advances in this field are fast. **InSAR GMS extensions in Arctic regions are foreseen in the future**. In the recent report of the Copernicus Polar Task Force (Duchossois et al., 2024), it is stated that "it is necessary to expend the EGMS over Arctic regions" (p.36). The development project of the InSAR Svalbard GMS is featured as an example (p.37–38), and the task force recommends to "follow these regional efforts to expand the EGMS across the polar regions" (p.38). For constraining permafrost modelling, large-scale InSAR processing could **focus on only two thawing seasons, of which one is exceptionally cold, and one is exceptionally warm.** This would allow to understand spatial patterns of ice content in the active layer (cold thawing season) and in the uppermost permafrost (warm thawing season), which could through spatial clustering be assimilated into permafrost models like CryoGrid for improved model simulations.

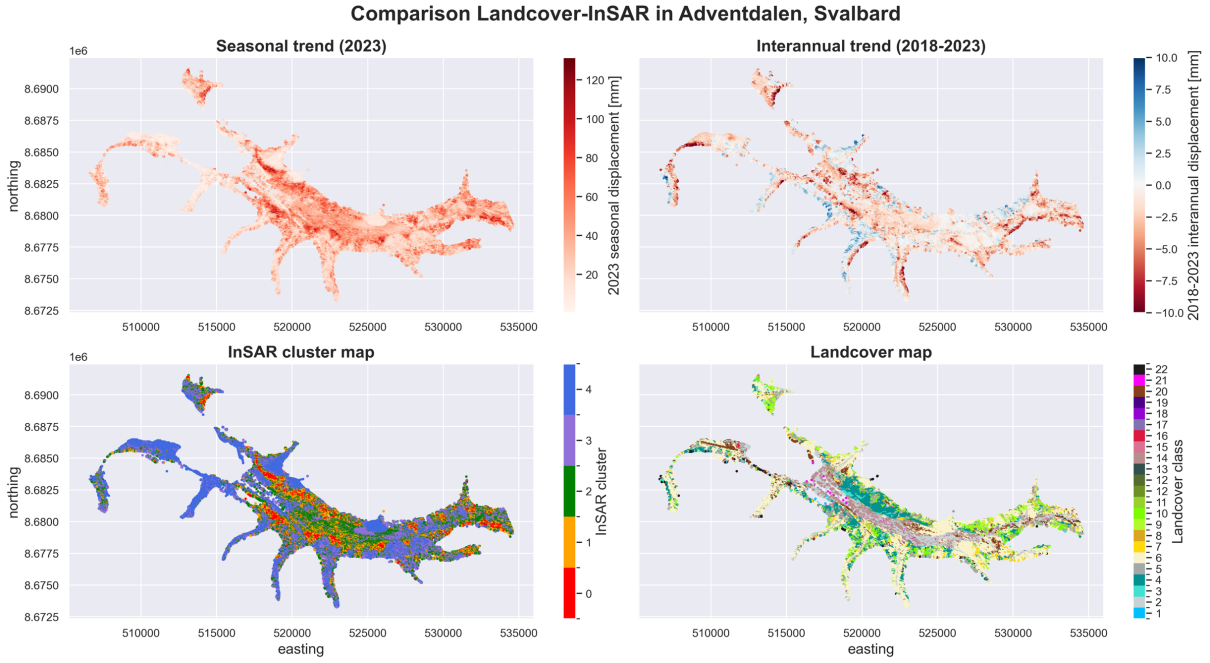

Figure 11: InSAR maps and landcover map for comparable area in Adventdalen. InSAR results further described in the CRDP [RD-1]. Landcover units from Bartsch et al. (2024a).

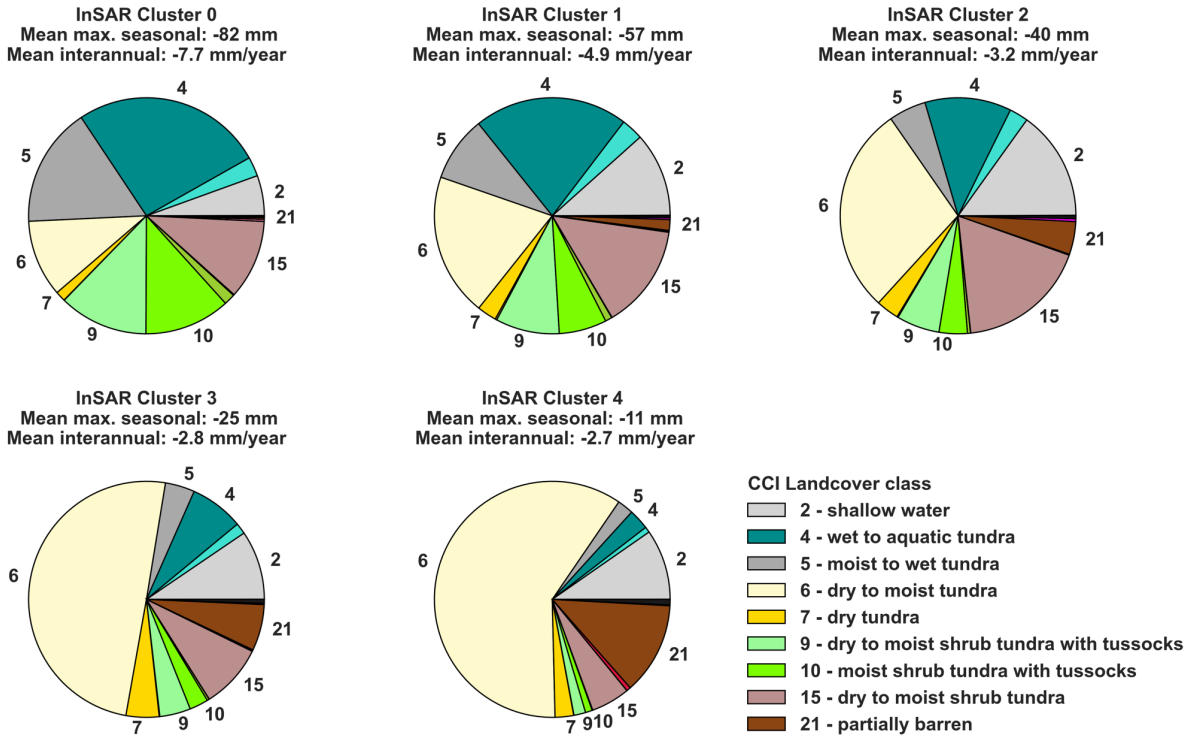

Figure 12: Comparison between InSAR clusters and landcover classes (Bartsch et al., 2024a).

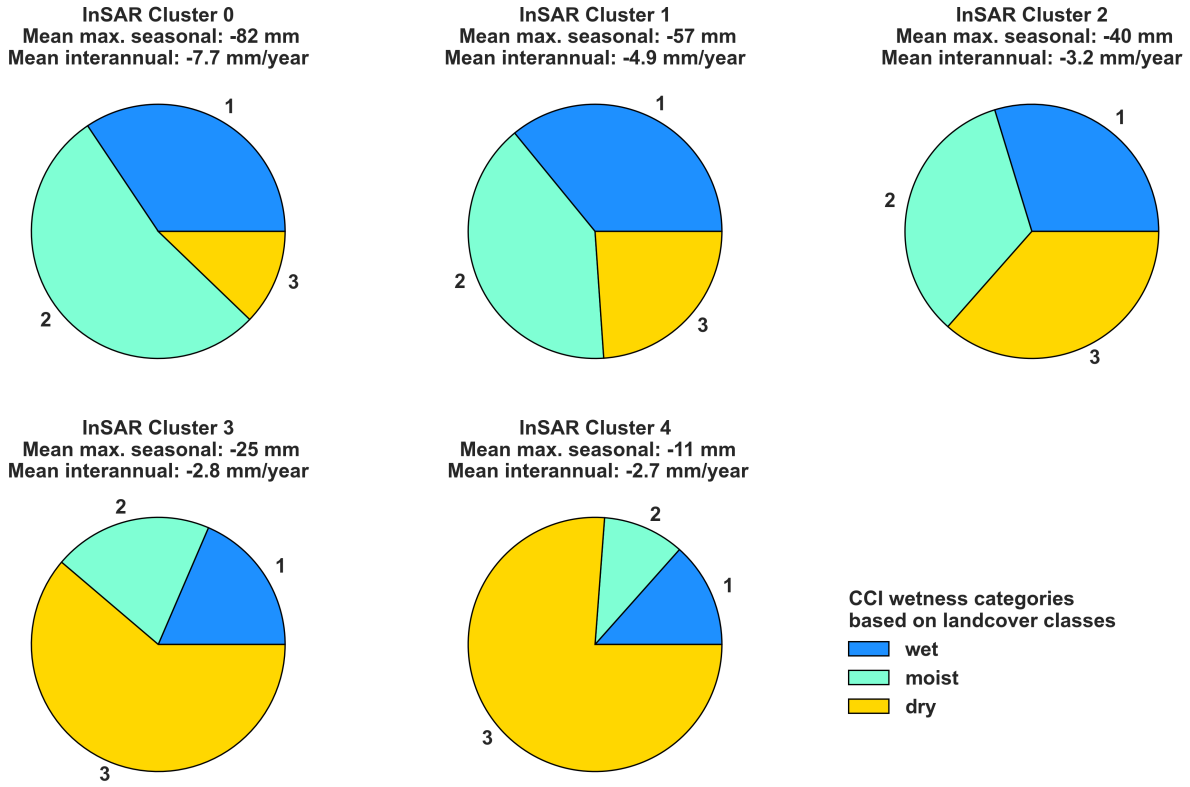

Figure 13: Comparison between InSAR clusters and landcover classes, grouped by wetness categories (according to Table 2 in Bartsch et al., 2024b).

7 References

7.1 Bibliography

Aalstad, K., Westermann, S., Schuler, T. V., Boike, J., and Bertino, L. (2018). Ensemble-based assimilation of fractional snow-covered area satellite retrievals to estimate the snow distribution at Arctic sites. *The Cryosphere*, *12*(1), 247–270. https://doi.org/10.5194/tc-12-247-2018.

Aga, J., Boike, J., Langer, M., Ingeman-Nielsen T., and Westermann S. (2023). Simulating ice segregation and thaw consolidation in permafrost environments with the CryoGrid community model. *The Cryosphere 17*(10), 4179–4206. https://doi.org/10.5194/tc-17-4179-2023.

Bamler, R., & Hartl, P. (1998). Synthetic aperture radar interferometry. *Inverse problems*, *14*(4), R1.

Bartsch, A., Efimova, A., Widhalm, B., Muri, X., von Baeckmann, C., Bergstedt, H., Ermokhina, K., Hugelius, G., Heim, B., Leibmann, M., and Khairullin, R. (2024a). Circumpolar Landcover Units (v1.1) [Data set]. Zenodo. https://doi.org/10.5281/zenodo.11486149.

Bartsch, A., Efimova, A., Widhalm, B., Muri, X., von Baeckmann, C., Bergstedt, H., Ermokhina, K., Hugelius, G., Heim, B. and Leibman, M. (2024b). Circumarctic land cover diversity considering wetness gradients. Hydrology and Earth System Sciences, 28(11), 2421-2481. https://doi.org/10.5194/hess-28-2421-2024.

Cigna, F., Esquivel Ramírez, R., and Tapete, D. (2021). Accuracy of Sentinel-1 PSI and SBAS InSAR Displacement Velocities against GNSS and Geodetic Leveling Monitoring Data. *Remote Sensing 13*, 4800. https://doi.org/10.3390/rs13234800.

Duchossois, G., Berdahl, M., Diehl, T., Garric, G., Humbert, A., Itkin, P., Jawak, S., and Tietsche, S. (2024). Copernicus polar roadmap for service evolution. Copernicus Polar Task Force. Publications Office of the European Union, Luxembourg. https://doi.org/10.2889/644108 .

Emardson, T. R., Simons, M., and Webb, F. (2003). Neutral atmospheric delay in interferometric synthetic aperture radar applications: Statistical description and mitigation. *Journal of Geophysical Research: Solid Earth 108*(B5). https://doi.org/10.1029/2002JB001781.

Jiang, J., and Lohman, R. B. (2021). Coherence-guided InSAR deformation analysis in the presence of ongoing land surface changes in the Imperial Valley, California. *Remote Sensing of Environment 253*, 112160, https://doi.org/10.1016/j.rse.2020.112160.

Li, Y., Zuo, X., Xiong, P., You, H., Zhang, H., Yang, F., Zhao, Y., Yang, Y., and Liu, Y. (2022). Deformation monitoring and analysis of Kunyang phosphate mine fusion with InSAR and GPS measurements. *Advances in Space Research 69*, 2637–2658, https://doi.org/10.1016/j.asr.2021.12.051.

Nitzbon, J., Gadylyaev, D., Schlüter, S., Köhne, J. M., Grosse, G., and Boike, J. (2022). Brief communication: Unravelling the composition and microstructure of a permafrost core using X-ray computed tomography. *The Cryosphere 16*(9), 3507–3515. https://doi.org/10.5194/tc-16-3507-2022.

Pumple, J., Monteath, A., Harvey, J., Roustaei, M., Alvarez, A., Buchanan C., and Froese D. (2024). Non-destructive multi-sensor core logging allows for rapid imaging and estimation of frozen

bulk density and volumetric ice content in permafrost cores. *The Cryosphere 18*(1), 489–503. https://doi.org/10.5194/tc-18-489-2024.

Subedi, R., Kokelj, S. V., and Gruber S. (2020). Ground ice, organic carbon and soluble cations in tundra permafrost soils and sediments near a Laurentide ice divide in the Slave Geological Province, Northwest Territories, Canada. *The Cryosphere 14*(12), 4341–4364. https://doi.org/10.5194/tc-14-4341-2020.

Wendt, L. (2024). Assessing ground ice changes in Svalbard from SAR interferometry and modelling. M.Sc. thesis. Department of Geoscience, Faculty of Mathematics and Natural Sciences, University of Oslo. http://hdl.handle.net/10852/112526.

Yalvac, S. (2020). Validating InSAR-SBAS results by means of different GNSS analysis techniques in medium- and high-grade deformation areas, *Environ. Monit. Assess. 192*, 120. https://doi.org/10.1007/s10661-019-8009-8.

Zwieback, S., Hensley, S., and Hajnsek, I. (2017). Soil Moisture Estimation Using Differential Radar Interferometry: Toward Separating Soil Moisture and Displacements. *IEEE Transactions on Geoscience and Remote Sensing 55*(9), 5069–5083. https://doi.org/10.1109/TGRS.2017.2702099.

7.2 Acronyms

AD	Applicable Document
ADP	Algorithm Development Plan
ALT	Active Layer Thickness
ATBD	Algorithm Theoretical Basis Document
B.GEOS	B.Geos GmbH
CAR	Climate Assessment Report
CCI	Climate Change Initiative
CRDP	Climate Research Data Package
ECV	Essential Climate Variable
EO	Earth Observation
ESA	European Space Agency
E3UB	End-To-End ECV Uncertainty Budget
GAMMA	Gamma Remote Sensing AG
GCOS	Global Climate Observing System
GMS	Ground Motion Service
GT	Ground Temperature
GTN-P	Global Terrestrial Network for Permafrost
UIO	University of Oslo
INSAR	Synthetic Aperture Radar Interferometry
IPA	International Permafrost Association
NORCE	Norwegian Research Centre AS
PE	Permafrost Extent
PF	Permafrost Fraction
PSD	Product Specification Document

PUG	Product User Guide
PVASR	Product Validation and Algorithm Selection Report
PVIR	Product Validation and Intercomparison Report
PVP	Product Validation Plan
RD	Reference Document
RMSE	Root Mean Square Error
SAR	Synthetic Aperture Radar
SD	Surface Displacement
SSD	System Specification Document
URD	Users Requirement Document
URq	User Requirement
WMO	World Meteorological Organisation